Journal of Solid State Chemistry 182 (2009) 1343–1350

Contents lists available at ScienceDirect

Journal of Solid State Chemistry

journal homepage: www.elsevier.com/locate/jssc

The $A^{2+}Mn_5(SO_4)_6$ family of triangular lattice, ferrimagnetic sulfates

D.V. West [a,*], T.M. McQueen [a], I.D. Posen [a], X. Ke [b], Q. Huang [c], H.W. Zandbergen [d], A.J. Williams [a], P. Schiffer [b], R.J. Cava [a]

[a] Department of Chemistry, Princeton University, Princeton, NJ 08544, USA
[b] Department of Physics and Materials Research Institute, Pennsylvania State University, University Park, PA 16802, USA
[c] NIST Center for Neutron Research, Gaithersburg, MD 20899, USA
[d] Kavli Institute for Nanoscience, Technical University of Delft, The Netherlands

ARTICLE INFO

Article history:
Received 5 February 2009
Received in revised form
24 February 2009
Accepted 1 March 2009
Available online 9 March 2009

Keywords:
Triangular lattice
Geometric frustration
Magnetism
Sulfate
Regular polygon tiling
Crystallography
New crystal structure

ABSTRACT

A new family of anhydrous sulfates, $A^{2+}Mn_5(SO_4)_6$ (A = Pb, Ba, Sr) is reported. The crystal structures of $PbMn_5(SO_4)_6$ and $SrMn_5(SO_4)_6$ are solved by powder X-ray and neutron diffraction. $BaMn_5(SO_4)_6$ is isostructural. $PbMn_5(SO_4)_6$ crystallizes with $P\bar{3}$ symmetry and unit cell parameters of $a = 14.551(1)$ Å and $c = 7.535(1)$ Å. The structure has rich features, including dimers of face-sharing MnO_6 octahedra, and two complementary triangular layers of Mn atoms. All compounds undergo a magnetic ordering transition at 10 K, below which, the magnetic susceptibility of the compounds varies systematically with the radius of the non-magnetic cation. Low temperature neutron diffraction shows that the complementary triangular layers result in a ferrimagnet with a net moment corresponding to one high spin Mn^{2+} per unit cell, correlating well with the magnetization data. The non-magnetic variant $PbMg_5(SO_4)_6$ is also reported.

1. Introduction

The study of magnetism on triangular lattices advances understanding of the sometimes complicated underlying physics of magnetic interactions [1–7]. Triangular geometry results in a special competition between forces that can frustrate primary interactions and therefore often allows weaker and longer range interactions to dominate magnetic behavior. While the majority of chemical research in this area focuses on the modification of existing structure types to understand the effects of dimension, inter-atom angles and magnetic orbital configuration on the magnetic interactions, the discovery of new triangular lattices can play an important role in opening new avenues for the study of the physics of magnetism.

Materials with tetrahedral polyatomic anions (e.g. SO_4^{2-}, PO_4^{3-}, MoO_4^{2-}, etc.) are candidates to find new triangular lattices. The number of such known compounds is far fewer than for oxides, perhaps owing as much to a lack of attention as to thermodynamics. Many of these compounds have a greater tendency than oxides to decompose at higher temperatures. Thus, the compounds studied have often been made at low temperatures, with many syntheses involving precipitation from aqueous solution and subsequent dehydration [8]. Yet some are rather resilient and can also be made with standard solid state techniques in a closed system at elevated temperatures [9,10].

In contrast to many oxides in which the strongly interacting magnetic cations are connected via direct metal–oxygen–metal bonds, when intervening sulfate groups are present the magnetic ions are typically separated by longer distances and thus have weaker interactions. These weaker interactions can provide the opportunity for a more detailed study of the magnetism under the relatively weak magnetic fields (<10 T) and temperature ranges (2–300 K) that are readily available in the laboratory. The current study reports the synthesis and the structural and magnetic characterization of a new family of sulfates with a unique, triangular arrangement of magnetic atoms and magnetic interactions strong enough to be significant, yet weak enough to be studied easily.

2. Experimental

All $A^{2+}Mn_5(SO_4)_6$ samples were made by intimately mixing stoichiometric quantities of $PbSO_4$, $BaSO_4$, $SrSO_4$, $MgSO_4$ and $MnSO_4 \cdot H_2O$ (Alfa Aesar). The mixed powders were dried in open quartz tubes at 440 °C under flowing N_2 gas for 2 h. To prevent rehydration, the tubes were evacuated and sealed immediately upon removal from the drying conditions. The mixtures were then

* Corresponding author. Fax: +1 609 258 6746.
E-mail address: barelytone@gmail.com (D.V. West).

0022-4596/$ - see front matter © 2009 Elsevier Inc. All rights reserved.
doi:10.1016/j.jssc.2009.03.001

heated for three days at 800 °C to yield single phase polycrystalline samples. Due to a lower rate of reaction, all materials containing Sr were heated at 900 °C. The Mg variant $PbMg_5(SO_4)_6$ was synthesized to provide a non-magnetic standard to aid in the interpretation of low temperature specific heat data. All samples are stable in air, but must be kept in a desiccator to avoid the gradual absorption of water.

Heat capacity and magnetic data were measured using Quantum Design Physical Property Measurement System (PPMS) and Superconducting Quantum Interference Device (SQUID) magnetometers. Heat capacities were measured in the range 0.3–100 K. Magnetization vs. temperature data were measured under 0.01 and 0.1 T fields in the temperature range 1.8–200 K. Magnetization vs. field curves were measured up to 9 T at 1.8 K. Susceptibility data were fit to the Curie–Weiss law from 50–200 K to obtain the Curie Weiss interaction temperature (θ_{CW}) and the effective magnetic moment (p_{eff}) values for the materials.

Nuclear and magnetic structures were characterized using X-ray, electron and neutron diffraction of polycrystalline samples. X-ray powder diffraction (PXRD) data were collected at room temperature with a Bruker D8-Focus, using Cu $K\alpha$ radiation with a graphite diffracted beam monochromator. TOPAS 2.0 (Bruker-AXS) was used for Rietveld refinement of PXRD data. The unit cell of $PbMn_5(SO_4)_6$ was auto-indexed using the TREOR algorithm [11]. Transmission electron microscopy (TEM) was performed with a Phillips CM 200 electron microscope equipped with a field emission gun. Neutron powder diffraction (NPD) data were collected on $PbMn_5(SO_4)_6$ and $SrMn_5(SO_4)_6$ at the NIST Center for Neutron Research on the high resolution powder neutron diffractometer (BT–1) with neutrons of wavelength 1.5403 Å produced by using a Cu(311) monochromator. Collimators with horizontal divergences of 15′, 20′ and 7′ of arc were used before and after the monochromator and after the sample, respectively. Data were collected at 5, 15 and 298 K for $PbMn_5(SO_4)_6$ and at 4, 20 and 298 K for $SrMn_5(SO_4)_6$ in the 2θ range of 3–168° with a step size of 0.05°. The structural parameters, both nuclear and magnetic, were determined by Rietveld refinement of the NPD data using the GSAS and EXPGUI programs [12,13]. The atomic neutron scattering factors used in the refinements for Pb, Mn, S, and O were 0.940, −0.375, 0.285, and 0.581×10^{-12} cm, respectively. The magnetic form factor coefficients used for Mn^{2+} were taken from the International Tables for Crystallography [14].

Due the large number of independent parameters, S–O bonds were restrained to a standard deviation of 0.006 Å around 1.474 Å, and all chemically similar atoms were constrained to have the same thermal parameters. For the magnetic refinement, the fit statistics were equally good when the moment vectors for the Mn^{2+} in the magnetically ordered state were constrained to the same magnitude and either parallel or anti-parallel to a given vector, or allowed to refine freely in magnitude and direction, attaining values comparable to the constrained refinement. As such, the constrained model is presented here.

3. Results and discussion

Crystal-chemical reasoning was employed to arrive at an initial structural model for compounds in this family. A single phase PXRD pattern was found for a 1:5 mixture of $PbSO_4$:$MnSO_4$ heated at 800 °C. Auto-indexing of this pattern gave a hexagonal unit cell with parameters $a = 14.55$ Å, $c = 7.55$ Å. The volume of the unit cell is expected to be close to an integer multiple of the sum of the volumes of the starting materials in the correct ratio. Dividing the volume of the indexed unit cell by the sum of the starting material volumes ($PbSO_4$+5$MnSO_4$) yields a value of 3.12. From this, we assigned a unit cell stoichiometry of $Pb_3Mn_{15}(SO_4)_{18}$. Using a triclinic unit cell with the indexed lattice parameters, a model was refined against the PXRD data with only the three Pb atoms in the unit cell. The strong X-ray scattering power of Pb allowed the phasing of the structure factors. Refinement of this Pb-only model placed the Pb atoms close to the 3-fold rotation axes of a hexagonal cell, with two near the *ab* faces, and one close to the middle of the 0 0 1 axis. As such, the Pb atom positions were fixed at the idealized positions of 0,0,1/2; 1/3,2/3,0 and 2/3,1/3,0. The fifteen Mn atoms were then initially placed between the Pb atoms to form a bi-layered unit cell (the cell dimension perpendicular to the hexagonal plane is that of approximately two face shared octahedra of large ions) containing nine metal atoms per layer. This arrangement forms two complementary hexagonal layers: one with seven Mn and two Pb atoms at $z = 0$, and another with eight Mn and one Pb at $z = 1/2$. Refinement of this Pb–Mn-only model retained the metal atoms close to their ideal positions, and gave a reasonable fit to the data.

Rietveld refinement against NPD data was used to locate the sulfates and finalize the structural model. The SO_4 tetrahedra were placed in the spaces of appropriate size and geometry between the layers of metal atoms. The initial refinements of the powder neutron data were performed in the space group *P*3. Close examination of the resulting structural model led to the final space group assignment of $P\bar{3}$. The final refinement in this space group yielded a crystal structure, with realistic bond lengths, angles, and coordination geometries (Fig. 1a), and an excellent fit to the NPD pattern (Fig. 2). The structural parameters for $PbMn_5(SO_4)_6$ are presented in Table 1. Detailed crystal structure analyses were also performed for $SrMn_5(SO_4)_6$, but not for the other reported family members, $BaMn_5(SO_4)_6$ and $PbMg_5(SO_4)_6$. Their unit cell dimensions, determined from fits to powder X-ray diffraction data (Fig. 3) taken at room temperature, are presented in Table 2. It is possible to mix the non-magnetic cations in a solid

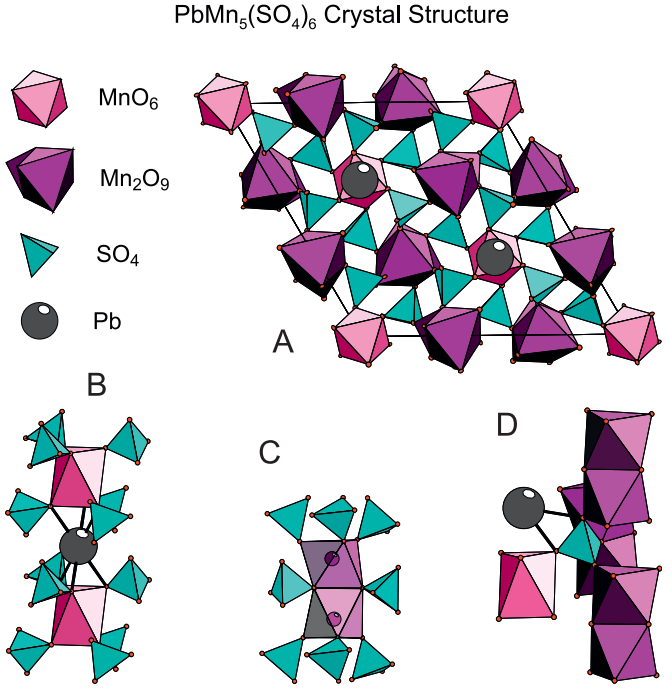

Fig. 1. The crystal structure of $PbMn_5(SO_4)_6$. The unit cell contains three formula units. (a) Full unit cell showing 1-D chains of alternating Pb–Mn along the 3 fold rotational axes (Pb atoms sit underneath MnO_6 octahedra at 0,0,1/2), and Mn_2O_9 dimer units and SO_4 tetrahedra in the remaining space. (b) Pb–Mn chain from the side showing isolated MnO_6 octahedron in pink. (c) Mn_2O_9 dimer in purple. (d) Each sulfate in the structure is chemically similar. For interpretation of the references to color in this figure legend, the reader is referred to the web version of this article.

solution, and the series $Sr_{1-x}Pb_xMn_5(SO_4)_6$ with $x = 0.25$, 0.50 and 0.75 was made. The unit cell parameters of these materials are also given in Table 2.

There are two interesting structural characteristics to consider in this new family of compounds: (1) the motifs that make up the structure and (2) the complementary bi-layered arrangement of metal atoms. Considering first the structural motifs, there are two building blocks from which this material is constructed. The first is a rather rare instance of an Mn_2O_9 dimer, made of face-sharing MnO_6 octahedra (Fig. 1c) and with Mn atoms displaced outward from the ideal octahedral centers. This type of dimer may be unique to this family, in that it contains Mn^{2+}, whereas other known examples of this motif contain Mn^{4+} [15]. There are six such dimers per unit cell. The second motif is a one-dimensional chain of alternating MnO_6–PbO_{12} polyhedra (Fig. 1b) running perpendicular to the hexagonal plane. There are three of these chains per unit cell made from the remaining cations (three Pb and three Mn atoms), located on the three 3-fold rotational axes. The chain at 0,0,z is offset by 0,0,1/2 from the chains at 1/3,2/3,z and 2/3,1/3,z. It is this offset that differentiates the two layers of the structure mentioned above. Lastly, all SO_4 tetrahedra are chemically similar: two of the four sulfate oxygens are shared with the outer vertices of Mn_2O_9 dimers, one is shared with a middle vertex of an Mn_2O_9 dimer, and the last is shared with an MnO_6 octahedron in a Pb–Mn chain (Fig. 1d).

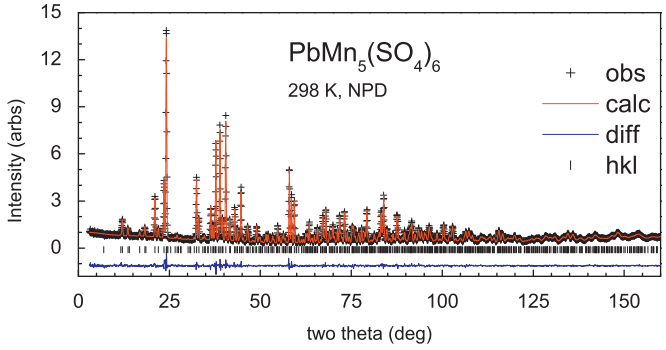

Fig. 2. Refinement of the crystal structure of $PbMn_5(SO_4)_6$ in the space group $P\bar{3}$ yields an excellent fit to the NPD data.

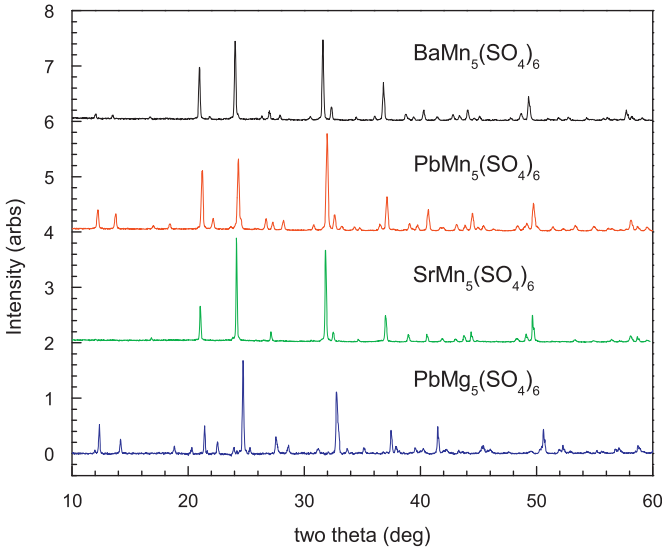

Fig. 3. X-ray powder diffraction patterns for single phase samples of the four members of the $A^{2+}Mn_5(SO_4)_6$ family.

Table 1
Refined structural parameters for $PbMn_5(SO_4)_6$ and $SrMn_5(SO_4)_6$ from NPD data.

Site	Atom	$PbMn_5(SO_4)_6$–298 K				$PbMn_5(SO_4)_6$–5 K				$SrMn_5(SO_4)_6$–298 K			
		x	y	z	B_{iso}	x	y	z	B_{iso}	x	y	z	B_{iso}
1*b*	Pb1/Sr1	0	0	1/2	1.92(6)	0	0	1/2	0.28(4)	0	0	1/2	2.1(2)
2*d*	Pb1/Sr2	1/3	2/3	0.998(2)	1.92(6)	1/3	2/3	1.002(1)	0.28(4)	1/3	2/3	0.993(2)	2.1(2)
1*a*	Mn1	0	0	0	1.7(1)	0	0	0	0.8(1)	0	0	0	2.6(2)
2*d*	Mn2	1/3	2/3	0.499(4)	1.7(1)	1/3	2/3	0.504(3)	0.8(1)	1/3	2/3	0.487(3)	2.6(2)
6*g*	Mn3	0.996(1)	0.652(1)	0.034(2)	1.11(6)	0.346(1)	0.998(1)	0.965(1)	0.36(6)	0.002(3)	0.661(2)	0.040(3)	1.2(1)
6*g*	Mn4	0.679(1)	0.677(1)	0.542(1)	1.11(6)	0.322(1)	0.003(1)	0.546(1)	0.36(6)	0.679(2)	0.672(2)	0.539(3)	1.2(1)
6*g*	S1	0.229(1)	0.094(1)	0.230(1)	0.66(7)	0.226(1)	0.097(1)	0.242(1)	0.30(5)	0.223(1)	0.096(2)	0.245(2)	0.86(9)
6*g*	O11	0.253(1)	0.039(1)	0.120(1)	1.96(3)	0.251(1)	0.036(1)	0.117(1)	0.7(2)	0.255(1)	0.049(2)	0.107(2)	2.52(6)
6*g*	O12	0.222(1)	0.056(1)	0.424(1)	1.96(3)	0.222(1)	0.057(1)	0.423(1)	0.7(2)	0.228(2)	0.050(2)	0.416(2)	2.52(6)
6*g*	O13	0.305(1)	0.212(1)	0.236(1)	1.17(3)	0.308(1)	0.211(1)	0.239(1)	0.3(2)	0.302(2)	0.211(2)	0.236(2)	1.14(6)
6*g*	O13	0.121(1)	0.084(1)	0.201(1)	1.72(4)	0.121(1)	0.086(1)	0.204(1)	0.56(3)	0.116(1)	0.086(1)	0.228(2)	1.66(9)
6*g*	S2	0.537(2)	0.102(1)	0.252(2)	0.66(7)	0.539(1)	0.107(1)	0.257(1)	0.30(5)	0.539(1)	0.107(2)	0.244(2)	0.86(9)
6*g*	O21	0.463(1)	0.086(1)	0.398(1)	1.96(3)	0.460(1)	0.087(1)	0.397(1)	0.7(2)	0.465(1)	0.093(1)	0.390(2)	2.52(6)
6*g*	O22	0.496(1)	0.110(1)	0.082(1)	1.96(3)	0.496(1)	0.111(1)	0.081(1)	0.7(2)	0.493(2)	0.110(2)	0.072(2)	2.52(6)
6*g*	O23	0.574(1)	0.029(1)	0.253(1)	1.17(3)	0.571(1)	0.025(1)	0.258(1)	0.3(2)	0.574(2)	0.027(2)	0.245(2)	1.14(6)
6*g*	O24	0.631(1)	0.213(1)	0.293(1)	1.72(4)	0.632(1)	0.214(1)	0.294(1)	0.56(3)	0.631(1)	0.212(1)	0.292(2)	1.66(9)
6*g*	S3	0.213(1)	0.448(1)	0.246(1)	0.66(7)	0.208(1)	0.442(1)	0.252(1)	0.30(5)	0.206(1)	0.441(1)	0.246(2)	0.86(9)
6*g*	O31	0.155(1)	0.444(1)	0.088(1)	1.96(3)	0.157(1)	0.447(1)	0.086(1)	0.7(2)	0.157(2)	0.441(2)	0.076(2)	2.52(6)
6*g*	O32	0.134(1)	0.412(1)	0.405(1)	1.96(3)	0.136(1)	0.414(1)	0.405(1)	0.7(2)	0.134(1)	0.424(1)	0.393(2)	2.52(6)
6*g*	O33	0.241(1)	0.362(1)	0.234(1)	1.17(3)	0.242(1)	0.362(1)	0.236(1)	0.3(2)	0.240(2)	0.360(2)	0.238(2)	1.14(6)
6*g*	O34	0.299(1)	0.547(1)	0.285(1)	1.72(4)	0.301(1)	0.547(1)	0.288(1)	0.56(3)	0.296(1)	0.547(1)	0.294(2)	1.66(9)
Lattice parameters													
	a (Å)		14.5514(2)				14.4847(1)				14.5938(5)		
	c (Å)		7.5348(2)				7.5248(1)				7.5185(3)		
Fit statistics													
	χ^2		1.68				2.33				1.82		
	$R(F^2)$ (%)		3.94				2.73				6.01		
	R_p (%)		3.67				4.56				4.98		
	Rw_p (%)		4.56				5.66				6.22		

Table 2
Comparison of lattice parameters.

Compound	a (Å)	c (Å)
$BaMn_5(SO_4)_6$	14.607(1)	7.599(1)
$PbMn_5(SO_4)_6$	14.551(1)	7.535(1)
$Sr_{0.25}Pb_{0.75}Mn_5(SO_4)_6$	14.530(1)	7.523(1)
$Sr_{0.50}Pb_{0.50}Mn_5(SO_4)_6$	14.527(1)	7.515(1)
$Sr_{0.75}Pb_{0.25}Mn_5(SO_4)_6$	14.511(1)	7.514(1)
$SrMn_5(SO_4)_6$	14.504(1)	7.519(1)
$PbMg_5(SO_4)_6$	14.417(1)	7.267(1)

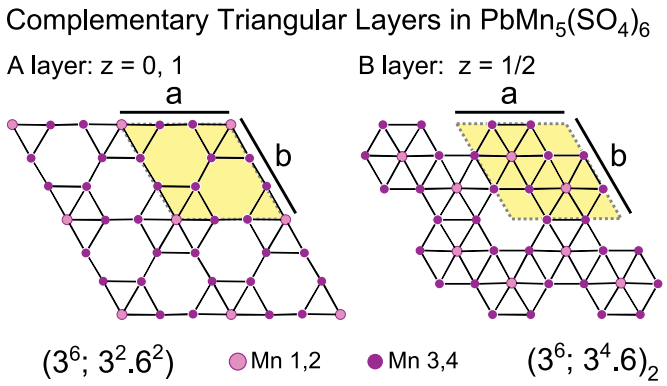

Fig. 4. Complementary cation layers. (a) The A cation layer, which sits at the *ab* faces of the unit cell, approximates the $(3^6;3^2\cdot6^2)$ regular polygon tiling. (b) The B cation layer, at $z\sim1/2$, approximates the $(3^6;3^4\cdot6)$ tiling. Mn atoms from the Pb–Mn chains occupy 3^6 sites within both planes, while dimer Mn atoms sit at the $3^2\cdot6^2$ (A layer) and $3^4\cdot6$ (B layer) sites.

The second structural characteristic to consider is the layered arrangement of cations. The unit cell has two layers, an A layer at $z\sim0$ that contains seven Mn and two Pb, and a B layer at $z\sim1/2$ with eight Mn and one Pb (Fig. 4). This cation arrangement is a consequence of the staggering of one of the Pb–Mn chains with respect to the other two. Considering only the magnetic Mn cations, the layers can be thought of as honeycomb lattices in which the A layer has one-third of the normally vacant sites within the honeycombs filled, whereas the B layer has two-thirds of the normally vacant sites in the honeycombs filled. The layers are stacked in a complementary fashion such that honeycombs that are empty in the A layer are filled in the B layer, and vice-versa. The "empty" honeycomb sites are actually occupied by non-magnetic Pb atoms. These layers approximate two of the twenty '2-uniform tilings' of regular polygons [16]. The A layer is the $(3^6;3^2\cdot6^2)$ tiling, while the B layer is the $(3^6;3^4\cdot6)_2$ tiling. In both layers, Mn atoms from the Pb–Mn chains occupy the 3^6 sites (i.e. a vertex shared by six adjacent triangles), while the dimer Mn atoms occupy the $3^2\cdot6^2$ sites in the A layer (a vertex shared by two adjacent triangles and two adjacent hexagons) and the $3^4\cdot6$ sites in the B layer (a vertex shared by four adjacent triangles and one hexagon).

Magnetic characterization of the compounds was performed via measurements of the magnetization vs. temperature and applied field (Figs. 5,8–10) for all samples. For the prototype compound, $PbMn_5(SO_4)_6$, the $1/\chi$ vs. T plot under a field of $\mu_0H=0.10\,T$ (Fig. 5) shows linear, Curie–Weiss behavior above 15 K with $\theta_{CW}=-18\,K$. The slope of the line yields $p_{eff}=5.9\,\mu_B$/Mn, consistent with the moment expected for high spin Mn^{2+} [17]. A phase transition is seen at 10 K as a drop in $1/\chi$ vs. T, and conversely an increase in susceptibility at that temperature (Fig. 5a). The nature of this magnetic transition can be seen further in the M vs. H curve at 1.8 K (Fig. 5b). The plot is

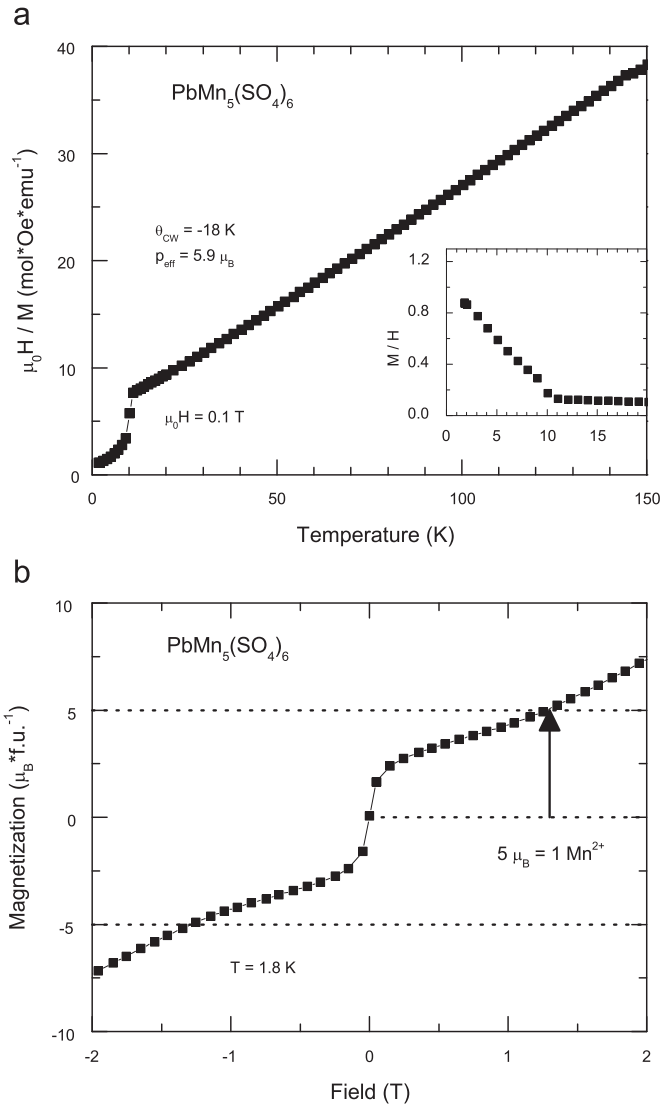

Fig. 5. $PbMn_5(SO_4)_6$ magnetic data. (a) $1/\chi$ vs. T plot showing magnetic ordering transition at 10 K. Inset: χ vs. T plot from 0–20 K. (b) Magnetization vs. field curves at 1.8 K. The saturation up to 1 T is equal to one Mn^{2+} moment per unit cell.

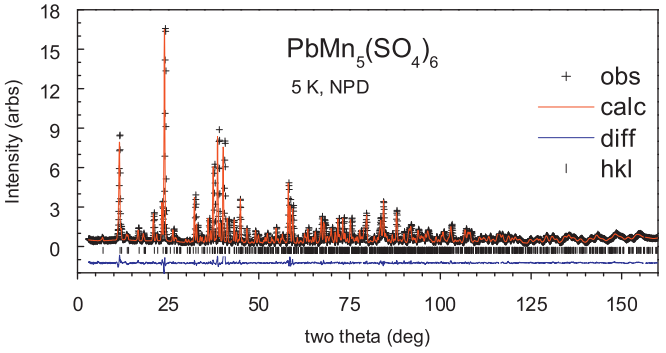

Fig. 6. Combined refinement of $PbMn_5(SO_4)_6$ nuclear and magnetic structures against NPD pattern at 5 K. The magnetic unit cell is the same as the nuclear unit cell with the space group $P\bar{1}$.

normalized to moment (μ_B) per unit cell, and shows a ferrimagnetic saturation of 5 μ_B per unit cell at $\mu_0H=1\,T$. This corresponds to exactly one $S=5/2$, Mn^{2+} per unit cell. After this saturation, linear M vs. H behavior is seen from $\mu_0H=1$–9 T. No hysteresis is observed in these M vs. H data.

To explain the observed magnetic properties, the magnetic structure was determined using NPD at 5 K, well below the phase transition. The magnetic reflections are indexable by a unit cell identical to that of the nuclear structure. Free refinement of the moments in the space group $P1$ yielded a magnetic structure that approximated ferromagnetic alignment within the A and B layers, and antiferromagnetic alignment between the layers. The best fit (Fig. 6) was obtained in the space group $P\bar{1}$ while constraining the moments to be the same magnitude and either parallel or antiparallel to a common vector (Fig. 7). The final refinement places the common vector canted 10(2)° off the *ab* plane with a magnitude of 4.49(4) μ_B. Although the refined vector is close to the [100] direction, the absolute orientation within the *ab* plane for trigonal space groups cannot be determined from powder data [18].

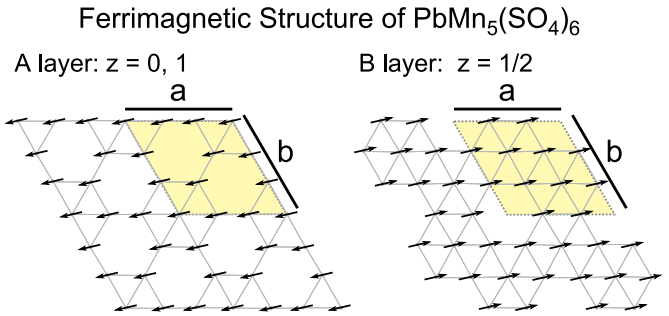

Fig. 7. Refined magnetic structure of $PbMn_5(SO_4)_6$. All moments are aligned ferromagnetically within the layers, and antiferromagnetically between the layers. The A layer has 7 Mn atoms for every 8 in the B layer, yielding a net moment of 5 μ_B/f.u. in the direction of the B layer moments.

This magnetic structure is perfectly consistent with the observed magnetic properties. The A layer has seven Mn^{2+} moments per unit cell aligned parallel to the common vector, while the B layer has eight moments per unit cell aligned antiparallel to the common vector. The result is a net moment of one Mn^{2+}, or 5 μ_B, per unit cell, accounting for the ferrimagnetic saturation seen in the M vs. H data, and also explaining the increase in the susceptibility below the phase transition.

That this is an oversimplified picture becomes apparent upon examination of the magnetic data for the rest of the compounds in the family. There is a trend in the magnetization data related to cation size. $BaMn_5(SO_4)_6$, being larger than the prototype compound, has very similar magnetization data (Fig. 8). In fact, the increase in susceptibility at 10 K is larger (Fig. 8a, inset), and the saturation plateau seen in M vs. H at low temperatures (Fig. 8b) is sharper than for $PbMn_5(SO_4)_6$. $SrMn_5(SO_4)_6$ on the other hand, with a somewhat smaller unit cell than the prototype compound, shows quite different behavior. The 10 K phase transition is not visible in the temperature-dependent susceptibility in an applied field of $\mu_0 H = 0.10$ T (Fig. 8) and no saturation is seen in the M vs. H data at low temperatures (Fig. 8, lower inset). It is only by magnetic measurements in a SQUID magnetometer, under a field of $\mu_0 H = 0.010$ T, that a magnetic phase transition at 10 K can clearly be seen for $SrMn_5(SO_4)_6$ in the χ vs. T data (Fig. 8, upper inset). Magnetic studies of the solid solution $Sr_{1-x}Pb_xMn_5(SO_4)_6$ show that the M vs. H saturation and the susceptibility increase at 10 K grow in with increasing Pb content (Fig. 9). The magnetic data shows that all family members have the transition at exactly the same temperature of 10 K, but

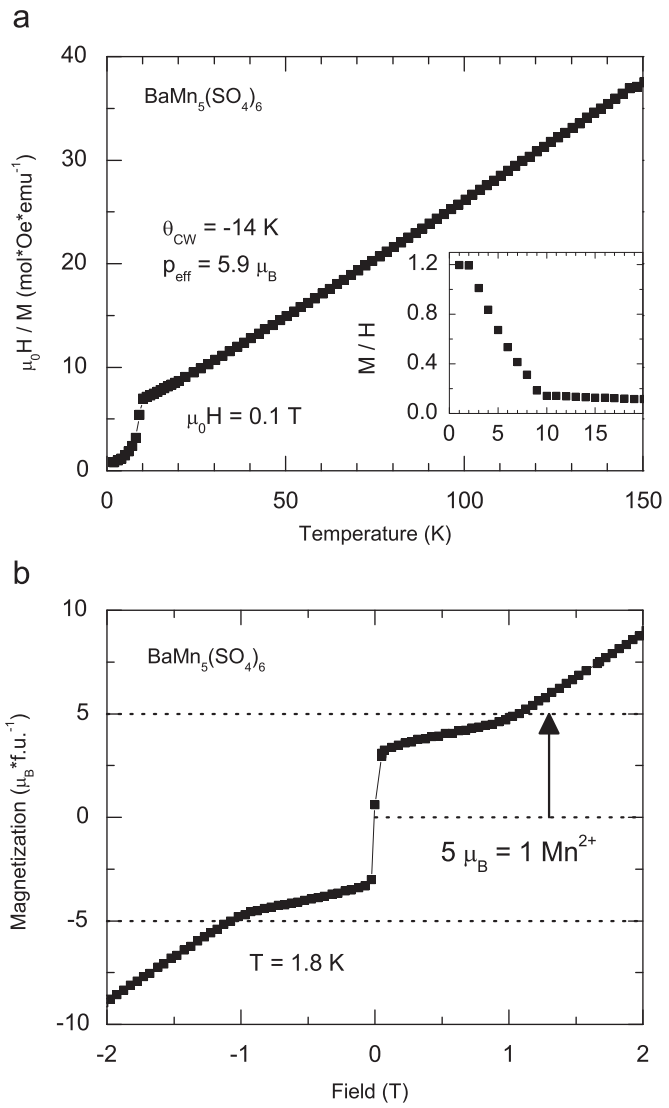

Fig. 8. $BaMn_5(SO_4)_6$ magnetic data. (a) $1/\chi$ vs. T plot, $\mu_0 H = 0.1$ T. (b) M vs. H at 1.8 K. Inset: χ vs. T plot from 0–20 K. Compared to $PbMn_5(SO_4)_6$, $BaMn_5(SO_4)_6$ has a sharper saturation in M vs. H and a greater rise in χ vs. T.

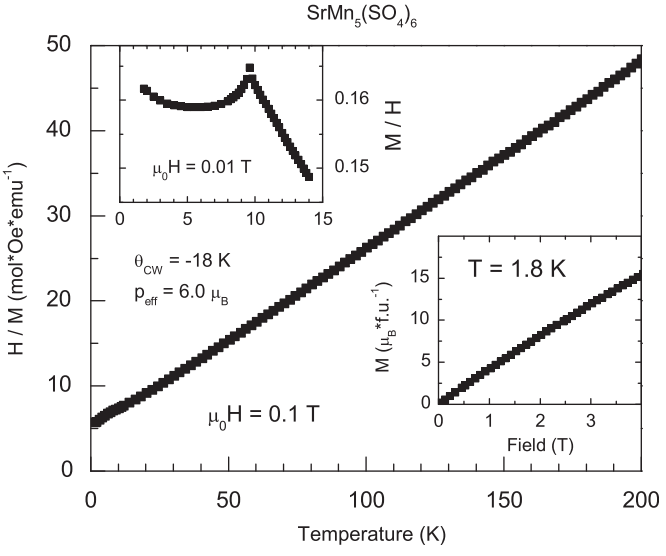

Fig. 9. $SrMn_5(SO_4)_6$ magnetic data. $1/\chi$ vs. T plot, $\mu_0 H = 0.1$ T. Upper inset: χ vs. T plot, $\mu_0 H = 0.01$ T, measured in the SQUID. Lower inset: M vs. H at 1.8 K. Contrary to the other members of this family, $SrMn_5(SO_4)_6$ shows no ferrimagnetic behavior, and the 10 K magnetic transition can only be observed in the SQUID with $\mu_0 H = 0.01$ T.

with a susceptibility below the transition that varies systematically with the radius of the non-magnetic cation (Fig. 10).

Specific heat measurements were performed on $PbMn_5(SO_4)_6$ and $SrMn_5(SO_4)_6$ to further elucidate the difference between their magnetic phase transitions. The data are shown in Fig. 11. The main panel shows the raw data for the magnetic samples in addition to the data from the non-magnetic analog $PbMg_5(SO_4)_6$ for which the observed specific heat arises only from phonon excitations. Nearly identical specific heat anomalies are observed at 10 K in the two compounds. This indicates that they lose their magnetic entropy in a similar fashion, despite their differences in low field susceptibility. By subtracting the heat capacity of the non-magnetic analog $PbMg_5(SO_4)_6$, the magnetic contribution to the specific heat can be estimated for the magnetic materials and the magnetic entropy can be quantified. The total entropy gain on heating is shown in the inset to Fig. 11. In spite of the approximations involved, within the error of the experiment, the magnetic entropy loss per mol Mn for both compounds reaches a limiting value near $R\ln(6)$, the value expected for high spin Mn^{2+}. The temperature dependence of the entropy changes is also similar: differences at temperatures above 20 K may be due to inaccuracy in the subtraction of the phonon contribution.

To further investigate the properties of $SrMn_5(SO_4)_6$, powder neutron and electron diffraction were employed. Rietveld refinement using the room temperature NPD pattern confirms that $SrMn_5(SO_4)_6$ has the $PbMn_5(SO_4)_6$ structure type (Table 1, Fig. 12). TEM diffraction images of the ($hk0$) and ($h0k$) planes, and a tilted image containing slices of the ($hk\bar{1}$), ($hk0$) and ($hk1$) planes (Fig. 13) show that $SrMn_5(SO_4)_6$ exhibits no signs of superstructure or disorder.

Subtracting the pattern above the magnetic transition from the one below, we can get an approximation of the magnetic only scattering in $PbMn_5(SO_4)_6$ and $SrMn_5(SO_4)_6$. Comparing these two difference patterns (Fig. 14), we see that they are nearly identical. Measuring the 0 0 1 magnetic intensity of $SrMn_5(SO_4)_6$ vs. temperature (Fig. 14 inset) confirms that long range order sets in at 10 K. Rietveld refinement against the $SrMn_5(SO_4)_6$ magnetic scattering yields the same magnetic structure as for $PbMn_5(SO_4)_6$. From their diffraction data and similarities in heat capacity, we can say that these two compounds have the same underlying magnetic structure at the level of the unit cell despite having dramatically different responses to a magnetic field.

Examining the structural and magnetic data from all compounds, a few speculations can be offered about the magnetic

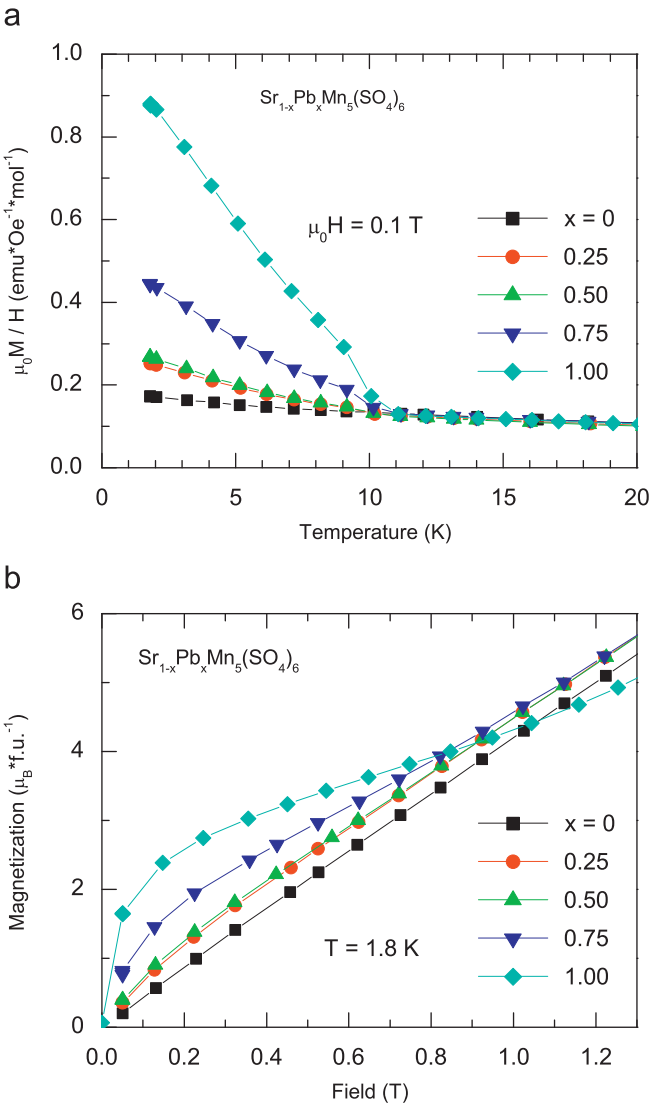

Fig. 10. Systematic variation of magnetic properties with cation radius. The spike in χ vs. T (a) and the saturation in the M vs. H curves (b) grow in with increasing substitution of Sr^{2+} with the larger Pb^{2+} cation.

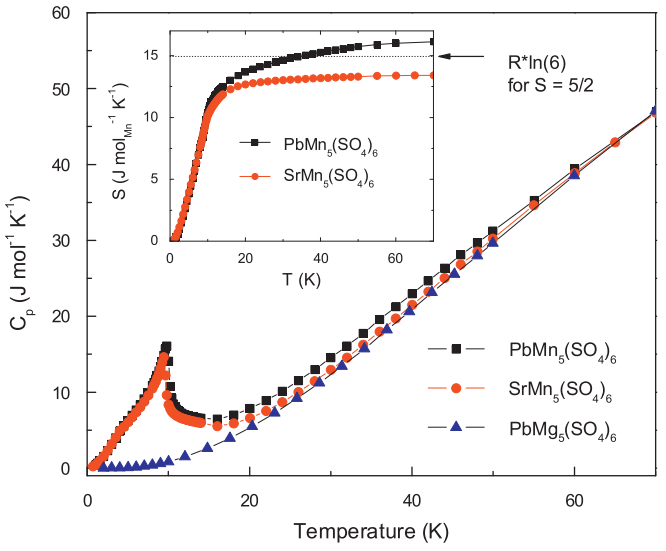

Fig. 11. Heat capacity. The Sr and Pb compounds both have identical anomalies in their specific heat curves. A phonon subtraction was attempted using $PbMg_5(SO_4)_6$ as the non-magnetic analog, but the cation mass differences are too large for an accurate assessment of the magnetic entropy loss. The inset indicates that within the error of the experiment, both compounds lose an entropy close to the expected value for an $S = 5/2$ magnetic ordering.

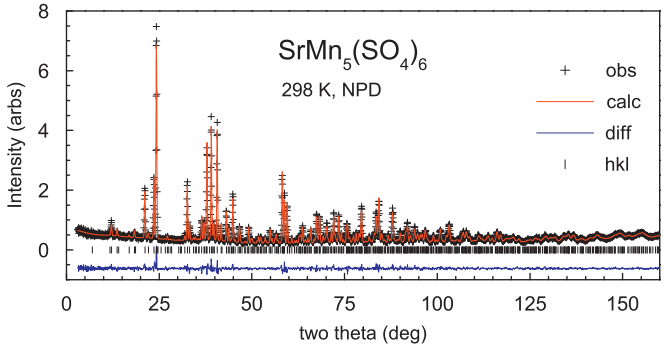

Fig. 12. Refinement against the NPD data for $SrMn_5(SO_4)_6$ at 298 K indicates that this member has the same nuclear structure as $PbMn_5(SO_4)_6$.

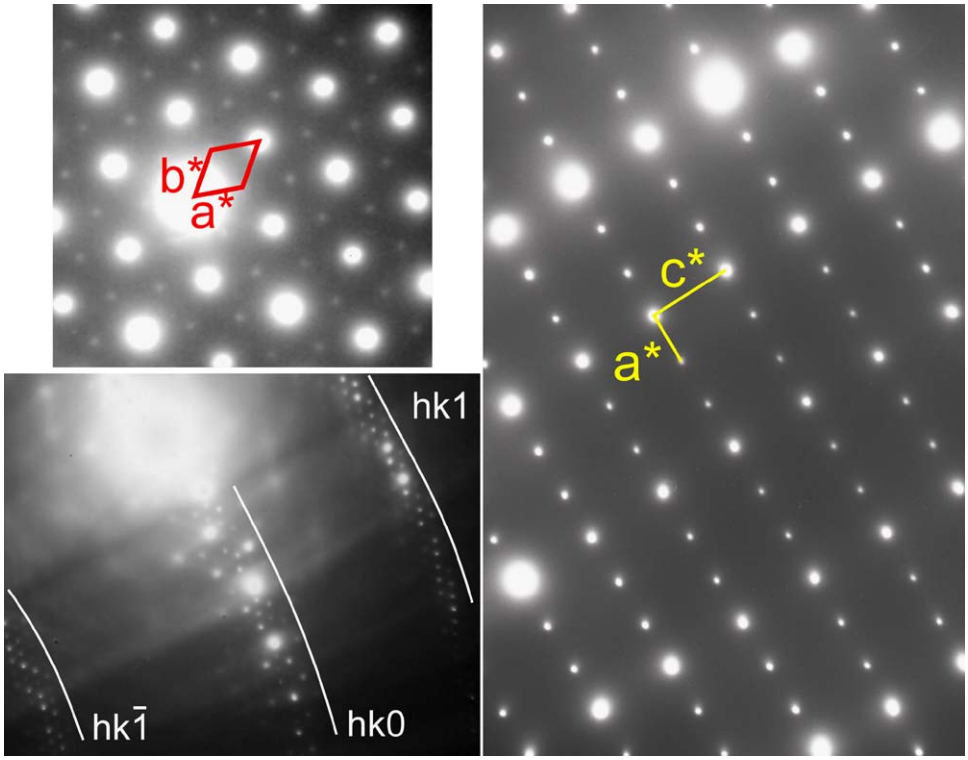

Fig. 13. TEM diffraction images of $SrMn_5(SO_4)_6$ showing the $h\,k\,0$ (upper left), $h\,0\,1$ (right) and simultaneous slices of the $h\,k\,\bar{1}$, $h\,k\,0$ and $h\,k\,1$ planes (lower left) indicate the correct unit cell with no signs of structural disorder.

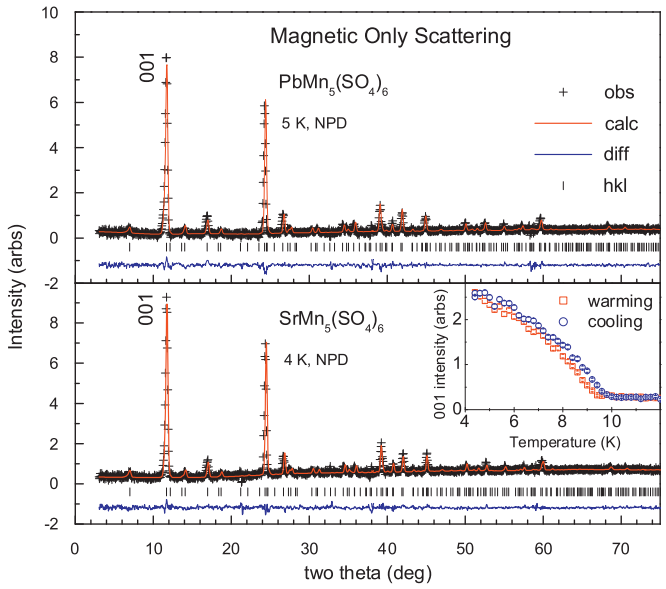

Fig. 14. Subtracting the patterns above and below the magnetic transition gives an approximation of the magnetic only scattering. Refinements of magnetic only models against these approximations show that the underlying magnetic structure is the same for both compounds (inset). The intensity of the magnetic 0 0 1 peak as function of temperature for $SrMn_5(SO_4)_6$.

properties. In all likelihood, the temperature of the magnetic phase transition derives from the magnetic interaction between the two Mn atoms in the Mn_2O_9 dimers. The evidence for this assertion is the invariant ordering temperature (10 K) for all compounds regardless of unit cell size. The non-magnetic cations have little effect on the Mn-Mn distance in the dimers (3.22(2) Å for $PbMn_5(SO_4)_6$, and 3.17(3) Å for $SrMn_5(SO_4)_6$ at 298 K). The differences below 10 K seen for the different members of this family, then, almost certainly involve the magnetic moments within the one-dimensional chains where the non-magnetic cations can exert the most influence. The data suggest a difference in interaction between moments across the non-magnetic cations. We attribute the absence of strong geometric magnetic frustration in these triangle-based compounds to the ferromagnetic in-plane interactions, which are not frustrating.

4. Conclusions

A new family of anhydrous sulfates has been discovered, and the structure of the prototype compound, $PbMn_5(SO_4)_6$, has been solved by powder X-ray and neutron diffraction. PXRD and NPD has shown that single phase samples with this structure type are similarly formed with Ba and Sr on the Pb site, and with Mg on the Mn site, and that a solid solution can be formed by mixing Sr and Pb statistically on the same site. Magnetic measurements and low temperature NPD have shown these compounds to be ferrimagnets owing to ferromagnetic planes of Mn^{2+} moments coupled antiferromagnetically to adjacent planes that have differing numbers of Mn^{2+}, resulting in a net magnetization in the direction of the planes with greater numbers of magnetic moments. The ordering temperature for all samples is equivalent in spite of differing unit cell sizes, prompting us to attribute the ordering temperature mostly to interactions within the rare Mn_2O_9 structural motif, interactions that are left relatively undisturbed by changes in the non-magnetic cation. The family shows a systematic trend in the magnetic susceptibility for the magnetically ordered state with non-magnetic cation radius. The difference may be attributable to a difference in magnetic interaction across the non-magnetic cations. Further investigation of these issues will require single crystal data.

Acknowledgments

This research was supported by the NSF grant number DMR-0701582, and by the NSF program in Solid State Chemistry, grant number NSF DMR-0703095. Certain commercial materials and equipment are identified in this report to describe the subject adequately. Such identification does not imply recommendation or endorsement by the NIST, nor does it imply that the materials and equipment identified are necessarily the best available for the purpose. T.M. McQueen gratefully acknowledges support of the National Science Foundation Graduate Research Fellowship Program.

Appendix A. Supplementary material

Supplementary data associated with this article can be found in the online version at doi:10.1016/j.jssc.2009.03.001.

References

[1] J.E. Greedan, J. Mater. Chem. 11 (2001) 37–53.
[2] P. Schiffer, A.P. Ramirez, Comm. Condens. Mater. Phys. 18 (1996) 21–50.
[3] A.P. Ramirez, Annu. Rev. Mater. Sci. 24 (1994) 453–480.
[4] H.T. Diep, Frustrated Spin Systems, World Scientific Publishing Company, Singapore, 2004.
[5] A.P. Ramirez, Handbook of Magnetic Materials, vol. 13, Elsevier, Amsterdam, 2001.
[6] A. Olariu, P. Mendels, F. Bert, B.G. Ueland, P. Schiffer, R.F. Berger, R.J. Cava, Phys. Rev. Lett. 97 (2006) 167203.
[7] M. Collins, O. Petrenko, Can. J. Phys. 75 (1997) 605–655.
[8] S. Oyetola, A. Verbaere, Y. Piffard, M. Tournoux, Eur. J. Solid State Inorg. Chem. 25 (1988) 259–278.
[9] J. Bernard, P. Couchot, C. R. Hebdomadaires Seances Acad. Sci. Ser. C 262 (1966) 209–212.
[10] D.V. West, Q. Huang, H.W. Zandbergen, T.M. McQueen, R.J. Cava, J. Solid State Chem. 181 (2008) 2768–2775.
[11] P. Werner, L. Eriksson, M. Westdahl, J. Appl. Crystallogr. 18 (1985) 367–370.
[12] A.C. Larson, R.B. Von Dreele, Los Alamos National Laboratory Report LAUR, 86-748, 2000.
[13] B.H. Toby, J. Appl. Crystallogr. 34 (2001) 210–213.
[14] I.S. Anderson, P.J. Brown, J.M. Carpenter, G. Lander, R. Pynn, J.M. Rowe, O. Shaerpf, V.F. Sears, B.T.M. Willis, in: International Tables for Crystallography, vol. C, third ed., Springer, Berlin, 2006, pp. 430–487.
[15] K. Kuroda, N. Ishizawa, N. Mizutani, M. Kato, J. Solid State Chem. 38 (1981) 297–299.
[16] B. Grunbaum, G.C. Shephard, Mater. Mag. 50 (1977) 227–247.
[17] N.W. Ashcroft, N.D. Mermin, Solid State Physics, Thomson Learning, USA, 1976.
[18] G. Shirane, Acta Crystallogr. 12 (1959) 282–285.